Journal of Molecular Structure 1277 (2023) 134807

Contents lists available at ScienceDirect

Journal of Molecular Structure

journal homepage: www.elsevier.com/locate/molstr

Copper Ferrite nanoparticles synthesised using a novel green synthesis route: Structural development and photocatalytic activity

P. Aji Udhaya[a,1,*], Awais Ahmad[b,1], M. Meena[c], M. Abila Jeba Queen[a], M. Aravind[d], P. Velusamy[e], Tahani Mazyad Almutairi[f], Abdallah.A.A. Mohammed[f], Shafaqat Ali[g,h,*]

[a] Department of Physics, Holy Cross College, Nagercoil, Tamil Nadu, India
[b] Departamento de Quimica Organica, Universidad de Cordoba, Edificio Marie Curie (C-3), Ctra Nnal IV-A, Km 396, Cordoba E14014, Spain
[c] Department of Physics, S.T. Hindu College, Nagercoil, India
[d] Department of Physics, National Engineering College, K.R Nagar, Kovilpatti, Tamil Nadu, India
[e] Department of Physics, Thiagarajar College of Engineering, Thiruparankundram, Madurai, Tamil Nadu 625015, India
[f] Department of Chemistry, College of Science, King Saud University, Riyadh 11451, Saudi Arabia
[g] Department of Environmental Sciences, Government College University, Faisalabad 38000, Pakistan
[h] Department of Biological Sciences and Technology, China Medical University, Taichung 40402, Taiwan

ARTICLE INFO

Article history:
Received 14 December 2021
Revised 28 September 2022
Accepted 13 December 2022
Available online 17 December 2022

Keywords:
$CuFe_2O_4$ nanoparticles
Ferrite
Green synthesis
Egg white
Rhodamine B

ABSTRACT

The copper ferrite nanoparticles, recognized for their ferromagnetic characteristics, minimal conductivity, and superior electrochemical stability, were synthesized by a facile auto combustion approach using egg white as fuel via a green synthesis route. $CuFe_2O_4$ nanoparticles' structural, morphological, and optical properties were examined. XRD is used to determine the phase formation, particle size, and lattice parameter of spinel ferrite. X-ray Diffractometer (XRD), Fourier Transform Infrared Spectrometer (FTIR), Scanning Electron Microscopy (SEM), and Energy Dispersive X-ray analysis were used to rigorously examine the phase purity of the synthesized spinel ferrite. For morphological analysis, SEM and TEM were employed, whereas EDAX was used for elemental analyses. For a better knowledge of the conduction band (CB) and valence band (VB) boundaries of the produced nanoparticles, optical experiments were conducted by UV Diffuse Reflectance Spectroscopy. The degradation of Rhodamine B dye determined the photocatalytic competence of the synthesized sample under visible light. At regular intervals of time, the entire process was observed with a spectrophotometer. $CuFe_2O_4$ nanoparticles reveal a maximum photocatalytic degradation efficiency of around 94%, which is higher than that of $CuFe_2O_4$ nanoparticles prepared via other chemical route.

1. Introduction

Wastewater management is a significant challenge in developing nations because of the numerous industrial processes that meet human needs. The dyeing and pigment industries are a significant source of non-biodegradable organic dyes in wastewater, which is a big worry for the environment. Humans use dyeing in a variety of applications, including textiles and food. Rhodamine B is an organic synthetic dye that is primarily water-soluble. Because of its luminous feature is used as a colouring agent in textiles, paper, plastics, cosmetics, leather, food, and many other sectors, resulting in significant dye effluent emissions. If effluents are not adequately handled, they pose a significant environmental risk to flora, fauna, and human health. Rhodamine B dye may cause cancer by irradiating the eyes and skin, as well as causing harm to the respiratory, reproductive, and neurological systems. Furthermore, Rhodamine B is harmful even at low concentrations, emphasizing the need for Rhodamine B wastewater treatment [1,2].

To detoxify Rhodamine B-containing water, photocatalytic degradation, ozonation, an electrochemical method, the Fenton process, and other processes were applied. Photocatalytic degradation is an emerging eco-friendly technique that uses light irradiation to generate electron and hole pairs in an aqueous solution. The photogenerated hole (h^+) combines with H_2O and OH to form the hydroxyl radical ($OH^\bullet$), which is an essential and efficient oxidising agent for the breakdown of such a hazardous dye [3].

Ferrites are ferrimagnetic materials composed chiefly of complex oxides containing ferric ions and are classified as magnetic materials due to their ferrimagnetic activity. The magnetic chattels of ferrite are caused by interactions between metallic ions at certain positions relative to oxygen ions in the oxide crystal struc-

* Corresponding authors.
E-mail address: shafaqataligill@yahoo.com (S. Ali).
[1] xxx

https://doi.org/10.1016/j.molstruc.2022.134807
0022-2860/

ture. From 1945 to 1993, Snoek and his colleagues at the Philips Research Laboratories in the Netherlands improved a variety of ferrites [4,5]. Based on the molar ratio of Fe_2O_3 to other oxide components and their crystal structure, ferrites are classified into four types [6]. The four groups are spinel ferrites, garnet ferrites, ortho ferrites, and hexagonal ferrites. Chemical stability, mechanical hardness, electromagnetic strength, and other features distinguish these ferrites.

$CuFe_2O_4$ nanoparticles are the desired spinel ferrite because their physical characteristics, such as phase transitions, electrical switching, semi-conductivity, magnetic properties, and chemical stability, may change when exposed to different environmental conditions [7]. $CuFe_2O_4$ nanoparticles appear in the form of inverse or mixed spinel ferrite. $CuFe_2O_4$ nanoparticles have been used as anode materials for lithium-ion rechargeable batteries, magnetic resonance imaging materials, photocatalysts for hydrogen evolution using visible light, energy storage materials, catalysts in nanomedicine for treating breast cancer, catalysts for coupling reactions, catalysts for CO_2 reduction, photoanodes for solar water oxidation, support for enzyme immobilisation, and photocatalysts [8]. This article investigates using $CuFe_2O_4$ as a photocatalyst for wastewater or water treatment. Spinel ferrite nanoparticles may be synthesised by co-precipitation, microemulsion sol-gel, citrate sol-gel, hydrothermal, the redox process, combustion, and other methods. Each of these synthesis techniques has advantages and disadvantages [9]. Maensiri et al. [10] described the white egg technique for producing spinel ferrite nanoparticles as a low-cost, environmentally friendly, and simple way of making transition metal-substituted ferrites. Because egg white is a precursor, the reaction's poisonous precursors and hazardous effluents may be reduced.

Ferrites are one of the most effective visible light-sensitive photocatalysts because they may directly destroy pollutants using readily available sunlight. In this regard, in our present inquiry, we sought to create $CuFe_2O_4$ nanoparticles utilising a single-step synthesis approach. Utilising it for wastewater retreatment is a vital option for water pollution prevention. Previously, copper ferrite nanoparticles were discovered to be a 75% effective photocatalyst for Rhodamine B dye [11]. To our knowledge, no other report of $CuFe_2O_4$ nanoparticles synthesised using egg white as a photocatalyst in a green synthesis procedure has been published.

2. Experimental procedure

2.1. Synthesis of $CuFe_2O_4$ nanoparticles

Copper ferrite nanoparticles were created using high-chemical purity ferric nitrate anhydrate, cupric nitrate hexahydrate, and freshly processed egg white. Country egg was used in the research. Fresh eggs were used to synthesize copper ferrite nanoparticles. Egg white is noted for its foaming and emulsification capabilities and being water-soluble, making it easy to interact with metal ions. Egg white is also a binding agent and gel for material shaping. To generate a homogeneous solution, mix egg white and double distilled water in a 3:1 ratio at room temperature for an hour. $Cu(NO_3)_2.6H_2O$ and $Fe(NO_3)_3.9H_2O$ are combined in a 1:2 mole ratio, dropped into the homogeneous egg white solution and rapidly agitated at room temperature for four hours. There are no pH modifications made throughout the procedure. The mixed solution was then dried by heating it on a hot plate at 80 °C for many hours. The powder was then calcined for 3 h at 600 °C to produce the final product [12–14].

2.2. Characterizations

Some techniques are X-ray diffraction, Fourier transforms infrared spectroscopy examination using KBr pellets, and High-resolution Scanning. Some techniques include Electron Microscopy, tunneling Electron Microscopy, Energy Dispersive X-ray Spectroscopy, and UV-Diffuse Reflectance. To investigate the copper ferrite nanoparticles, spectroscopy was used. The crystallite phase of copper ferrite was established using the XPERT PRO diffractometer. The Fourier Transform Infrared analysis was captured using a Bruker IFS66V FT-IR spectrometer. The morphology of the prepared sample was examined using High-Resolution Scanning Electron Microscopy and tunneling Electron Microscopy. The optical parameter was measured using a UV-DRS Spectrometer. Under visible light irradiation, the photocatalytic activity of $CuFe_2O_4$ nanoparticles for the degradation of Rhodamine B in an aqueous solution was evaluated.

3. Results and discussion

3.1. X-ray diffraction analysis

The XRD pattern of copper ferrite nanoparticles is exposed in Fig. 1. The XRD pattern reveals the crystalline nature of nanoparticles. The Braggs reflection plane announces the formation of the cubic spinel structure. The diffraction peaks were obtained at 29.7°, 33.6°, 43.4°, 52.6°, 57. 33°, and 63.2° correspond to similar Braggs reflection planes of (220), (311), (400), (422), (511), and (440), respectively. The observed peaks were well matched with standard JCPDS Card No: 73–2317. The cubic ferrite nanoparticles reflection planes showed more intensity than the copper peak [15–17]. The minor rise obtained at 39.2° represents the presence of Cu nanoparticles. The lattice parameter of the copper ferrite nanoparticles is $a = 8.337 + 1$ Å using UNIT CELL software. The crystallite size of $CuFe_2O_4$ is determined using the Scherer formula [18]. $CuFe_2O_4$ nanoparticles reveal crystallite size values of 37 ± 3 nm for the maximal intensity peak in the (311) plane.

$$D = \frac{k\lambda}{\beta cos\theta} \quad (1)$$

where 'D' stands for particle size, 'λ' stands for X-ray beam wavelength, 'β' and 'θ' stand for full width half maximum and Bragg's diffraction angle of the associated peak, respectively, and 'k' stands for the instrumental constant. The X-ray density (P_x) is calculated using the following formula: 5.484 g/cc.

$$P_x = \frac{8M}{Na^3} \quad (2)$$

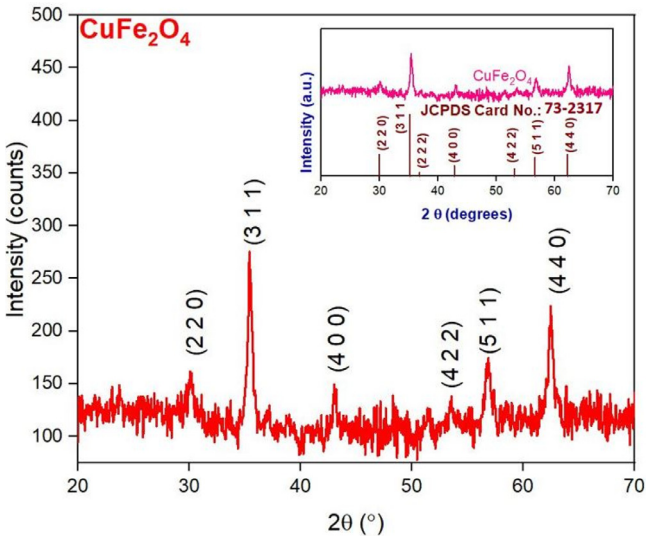

Fig. 1. XRD pattern of $CuFe_2O_4$ nanoparticles.

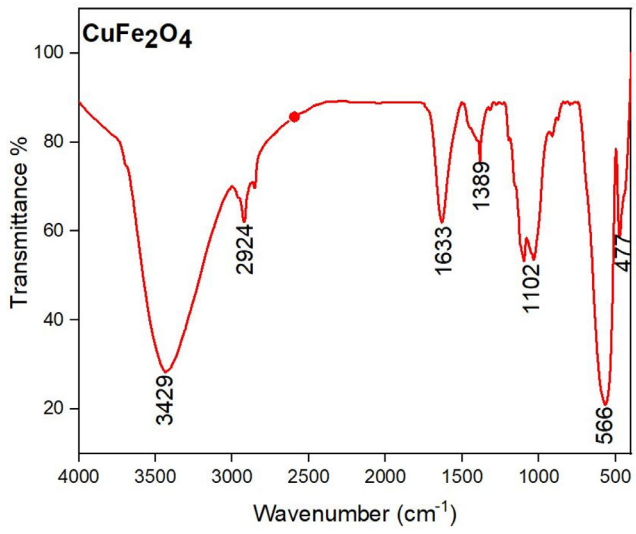

Fig. 2. shows FTIR spectra of $CuFe_2O_4$ nanoparticles.

The molecular weight, Avogadro number, and lattice constant is represented by M, N, and a, respectively. The distance between magnetic ions is measured by the hopping lengths d_A and d_B of tetrahedral and octahedral sites.

$$d_A = 0.25a\sqrt{3} \tag{3}$$

$$d_B = 0.25a\sqrt{2} \tag{4}$$

the values of hopping length are found using the above formulas [16] as $d_A = 3.626$ Å and $d_B = 2.961$ Å.

3.2. Fourier transform infrared analysis (FT-IR)

FTIR was used to determine the involvement of functional group interactions between metal nanoparticles and biomolecules. The egg white biomolecules are responsible for capping and stabilising the nanoparticles. FT-IR confirms the formation of the spinel structure in $CuFe_2O_4$ nanoparticles. The FT-IR spectra of copper ferrite nanoparticles in the wave number range of 4000 to 400 $cm^{-1}$are shown in Fig. 2.

The -OH stretch of the proteins in the egg white extract correlates to the sharp band found at 3429 cm^{-1}. The C–H stretching vibrations of methyl, methylene and methoxy groups are responsible for the peak at 2924 cm^{-1}. The 1633 cm^{-1} peak corresponds to C=O stretching in the carboxyl group or C=N bending in the amide group. The carboxylate group (CO_2^-) stretching vibration can be detected in the bands at 1389 cm^{-1} and 1102 cm^{-1}, which are connected to the nitrate ion traces. The FT-IR spectra were consistent with those previously reported for egg white-assisted silver nanoparticles [19]. The scope displays two wide metal-oxygen bands, the upper one (u1) in the 566 cm^{-1} range generated by stretching vibrations of the tetrahedral metal-oxygen [Fe-O] band and the lower one (u_2) in the 477 cm^{-1} range caused by metal-oxygen [Cu-O] beats in the octahedral sites. The force constants KT and KO values for the corresponding frequencies u1 and u2 of the $CuFe_2O_4$ A- and B-sites are calculated as 2.34 Nm^{-1} and 1.66 Nm^{-1}, respectively, using the formulae below.

$$K_T = 4\pi c^2 \nu_1^2 \mu \tag{5}$$

$$K_O = 4\pi c^2 \nu_2^2 \mu \tag{6}$$

where c is the speed of light, υ_1 and υ_2 are the frequencies of vibration of the A- and B-sites, and μ is the reduced mass of the Fe^{3+} and O^{2-} ions, which is nearly equivalent to 2.065×10^{-23}g [20].Because of the Coulomb force, molecules of different biomolecules and proteins will adsorb on NPs, generating electrostatic double layers and controlling particle size. Due to the Van der Walls force of attraction, the adsorption of multiple layers of biomolecules surrounding this electrostatic double layer led to the creation of a diffuse double layer. Because of the variability in the biomolecules contained in egg white, steric, electrostatic barriers form around the surface of nanoparticles. As a result, this may have aided in capping the NPs, preventing agglomeration, strengthening the stability, and promoting.

3.3. HR-SEM analysis

The morphology of the produced copper ferrite nanoparticles is examined using HR-SEM. Fig. 3 $CuFe_2O_4$ nanoparticles at a magnification of 500 nm are shown in Fig. 3. The average particle size was between 15 and 45 nanometers. Using ImageJ software and considering as many particles as possible from the micrograph in Fig. 3. The accumulation occurs due to the magnetic nature of ferrite nanoparticles and the binding of initial particles held together by weak surface contacts such as the Van der Waals force.

3.4. TEM analysis

Transmission electron microscopy was used to image the size and form of $CuFe_2O_4$ nanoparticles (TEM). Fig. 4 shows TEM images of $CuFe_2O_4$ nanoparticles at different magnifications and the SAED pattern. The vast majority of nanoparticles were shown as aggregates with oval or irregular shapes. The particle size distribution derived by Gaussian fit shows that the particle size ranges between 8 and 20 nm. The twinned particles were discovered by demonstrating brightness in one component of the particles compared to the other. Twining occurs when two subgrains share the same crystallographic plane. The presence of the (311) plane in the SAED pattern showed that the $CuFe_2O_4$ NPs were twinned. The diffraction patterns observed in a specific region reflect crystal structure and phase, which fit closely with the system of spinel ferrites. The superimposition of a bright area with a Debye ring pattern in the SAED pattern shows that the $CuFe_2O_4$ nanoparticles are polycrystalline, confirming the creation of a single phase of $CuFe_2O_4$ nanoparticles [21].

3.5. EDX analysis

The components contained in copper ferrite nanoparticles are investigated using EDX spectra. The EDX spectra of $CuFe_2O_4$ are shown in Fig. 5. Peaks at around 6.39 eV and 7 eV suggest the existence of iron in copper ferrite nanoparticles. The peak in the spectra at approximately 0.5 eV indicates the presence of oxygen. The peaks show the presence of copper in Fig. 5 at 0.9 eV, 8 eV, and 8.9 eV [22].

3.6. UV-DRS analysis

UV-visible DRS measurements were used to calculate the band gap of the $CuFe_2O_4$ nanoparticles. The Tauc relation was used to compute the band gap. To convert diffuse reflectance to absorption coefficient, the Kubelka-Munk function [23] was employed in combination with Eq. (8):

$$(huF(R\infty))^2 = A(hu - E_g) \tag{7}$$

where h is the Planck's constant, ν is the frequency,
E_g is the optical band gap energy,
A is the proportionality constant

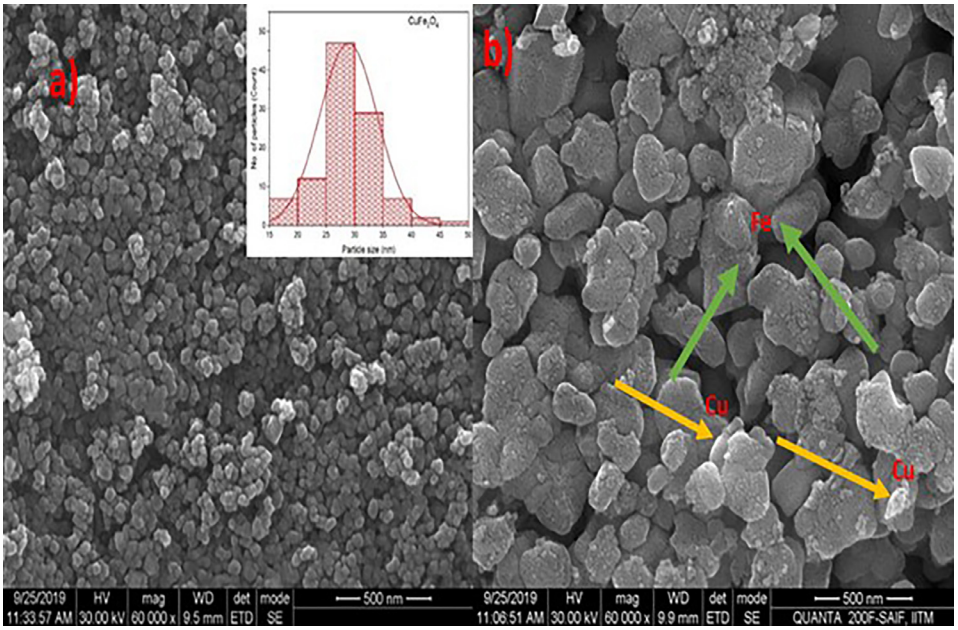

Fig. 3. Surface morphology and particle size distribution of $CuFe_2O_4$ nanoparticles from HRSEM.

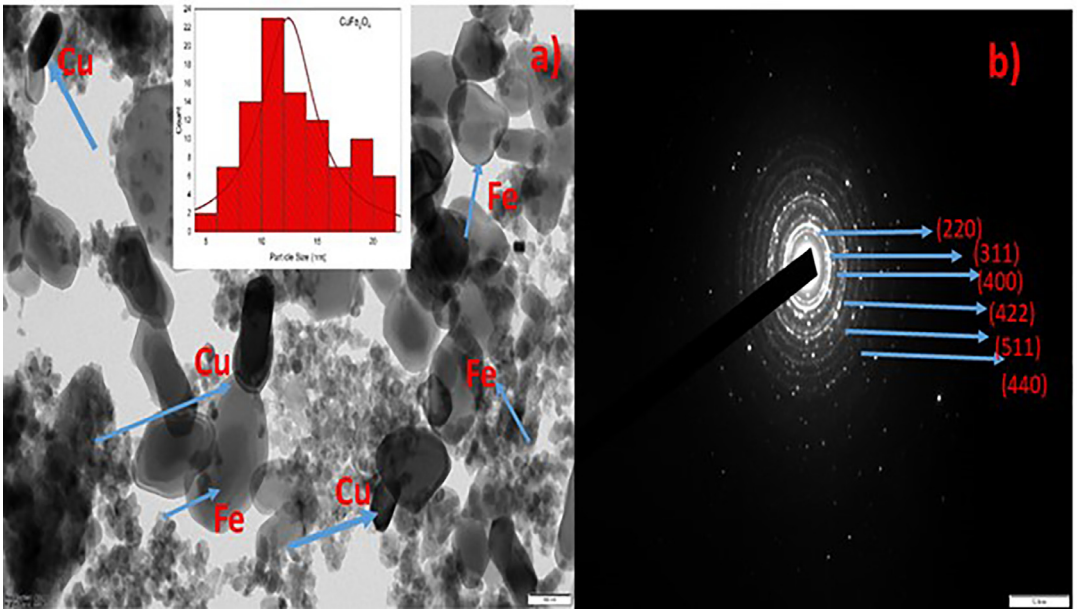

Fig. 4. (a) Surface morphology and particle size distribution of $CuFe_2O_4$ from TEM. (b) SAED pattern of $CuFe_2O_4$ nanoparticles.

F(R∞) is the function of Reflectance

$$F(R\infty) = \frac{(1-R)^2}{2R} \tag{8}$$

Where $n = 2$ implies a direct transition with a direct band gap, and $n = 1/2$ denotes an indirect transition with an indirect band gap. The band gap shown in Fig. 6 is the intercept produced by graphing $(F(R)h)_2$ vs the band gap (h). $CuFe_2O_4$ nanoparticles have an estimated band gap of 1.83 eV. The band gap of pure copper ferrite was discovered to be less than that of bulk $CuFe_2O_4$ nanoparticles (3.35 eV). This reduction in band gap might be caused by various factors, including impurities, carrier concentrations, crystallite size, and lattice strain [24].

The band edge positions of $CuFe_2O_4$ nanoparticles were estimated using equations [25].

$$E_{CB} = X - E^C - 0.5E_g \tag{9}$$

$$E_{VB} = E_{CB} + E_g \tag{10}$$

Where χ is the absolute electronegativity and is represented as the geometric mean of the absolute electronegativity of the component atoms. Which is defined as the arithmetic mean of the initial ionisation energy and the atomic electron affinity, normal Hydrogen Scale (NHE) (4.5 eV). Eq. (10) is the copper ferrite samples' energy band gap, and EC is the free electron energy on the ordinary hydrogen scale.

3.7. Photocatalytic degradation

As a catalyst, 6 mg of $CuFe_2O_4$ nanoparticles were scattered in 1 litre of Rhodamine B solution. The pH of the solution was adjusted to 2.0 using hydrochloric acid, and as is well known, an

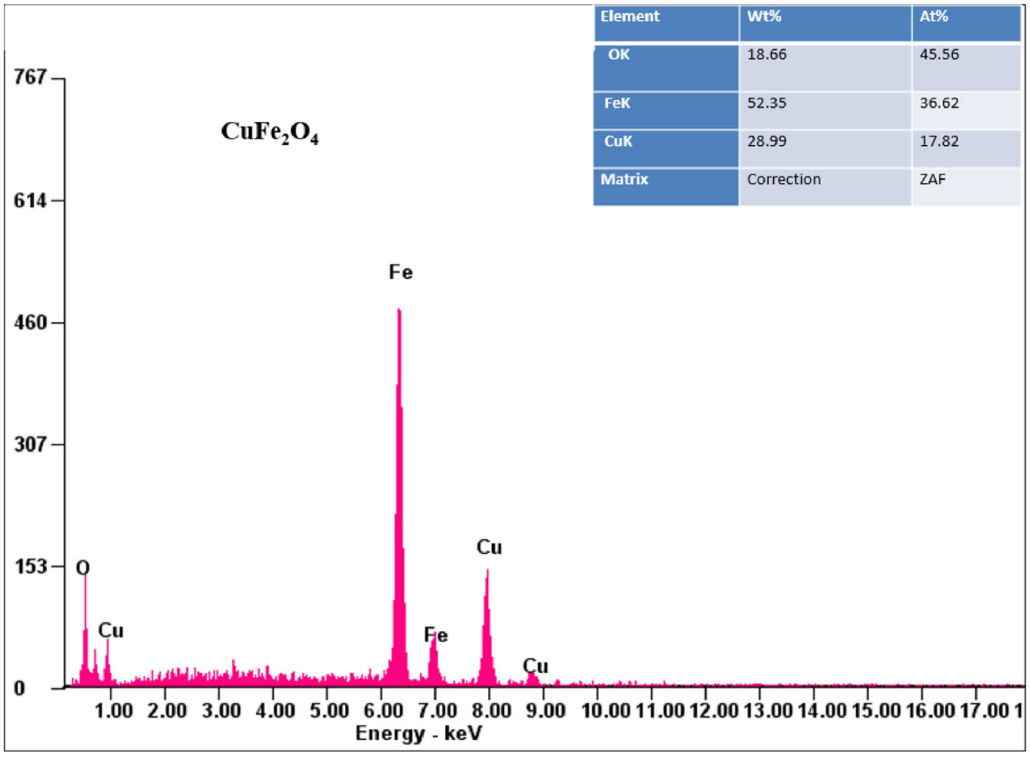

Fig. 5. EDX spectra of $CuFe_2O_4$ nanoparticles.

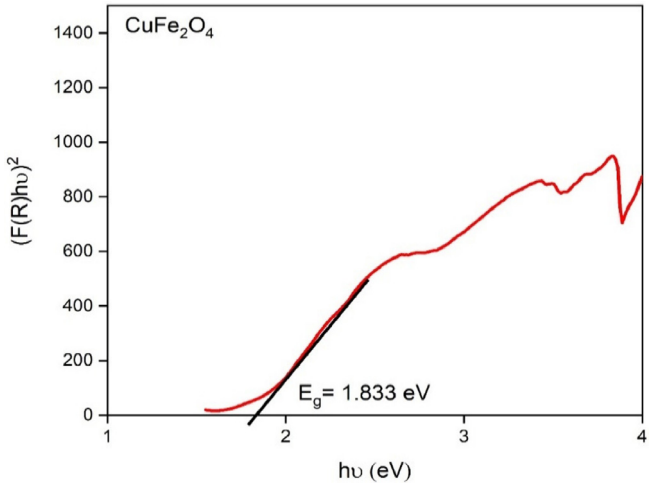

Fig. 6. Tauc Plot of $CuFe_2O_4$ nanoparticles.

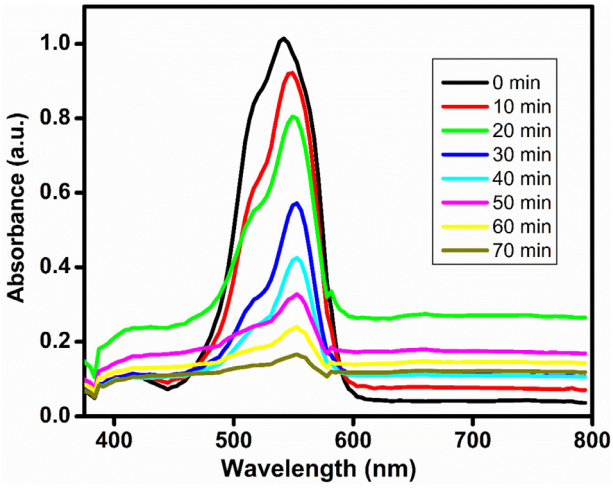

Fig. 7. Schematic Diagram of Experimental setup for Photocatalysis shows photocatalytic degradation of Rhodamine Blue dye.

acidic environment causes a Fenton reaction-like process to occur, and the solution suspension was kept in the dark overnight at room temperature to attain adsorption equilibrium. A 150 W halide lamp is then used to expose the suspension to visible light (>420 nm). During photoreaction, the air was purged from the solution to keep the cobalt ferrite catalyst well dispersed, and 0.1 mL of 30% H_2O_2 was added to the 1 L Rhodamine B solution to accelerate and create more $OH^{\bullet}$ radicals during photodegradation, resulting in the rapid formation of oxidation contaminates [26,27]. A UV-Visible spectrometer was used to determine the amount of Rhodamine B in aqueous solution before and after photodegradation in aliquots (1 ml) collected at various intervals. Fig. 7 depicts a schematic experimental setup for photocatalytic degradation.

3.7.1. Mechanism of dye degradation

Once $CuFe_2O_4$ nanoparticles are illuminated with visible light, electron-hole (e^-/h^+) pairs are formed, as seen in Fig. 8. Rhodamine B reduction and oxidation in an aqueous solution are aided by electron-hole pairs. The valence band edge (VB) in the sample is 2.226 eV, and the conduction band edge (CB) is at 0.436 eV against NHE. The CB edge for this system is less negative than the redox potential of $O_2/O_2\bullet$ (0.33 V). This prevents the electron in the CB from interacting with molecular oxygen to form superoxide anion radicals ($O_2\bullet$), equally powerful oxidants. As a result, the reduction process cannot take place. Hence, electrons on the $CuFe_2O_4$ conduction band surface react with additional hydrogen peroxide (H_2O_2) to form more $OH^{\bullet}$ radicals, resulting in the fast oxidation of Rhodamine B dye molecules.

Furthermore, the positive hole ($h+$), which has a more significant oxidation potential, can contribute to the direct oxidation of

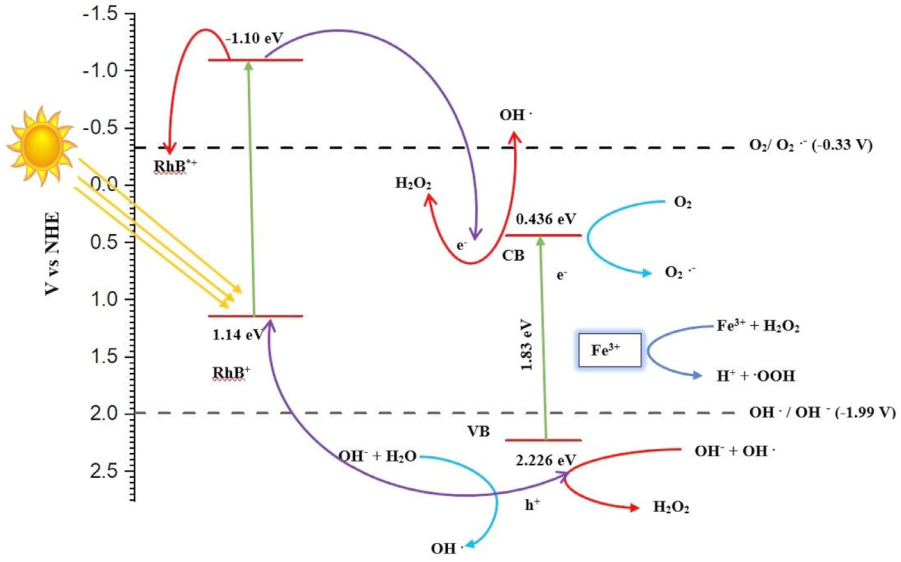

Fig. 8. Mechanism of Photocatalytic degradation of Rhodamine B by $CuFe_2O_4$nanoparticles.

Rhodamine B dye molecules. Compared to the redox potential of $OH^{\bullet}$/ OH, the VB edge of copper ferrite is more favourable (1.99 V). These holes can oxidise water by reacting with hydroxide ion (OH) to create an $OH^{\bullet}$ radical, causing a substantial blue shift in the peak position due to the de-ethylation of Rhodamine B molecules, as illustrated in Fig. 8. The photocatalytic routine of the sample with the contact time was determined from the expression below:

$$\eta = \frac{A_o - A}{A_o} \times 100\% \quad (12)$$

where η is the removal efficiency, A_o is the initial absorbance and A is the variable absorbance.

The findings showed that the absorbance of the solution decreases with increasing time intervals, meaning that the dye concentration decreases with increasing exposure time [28,29]. The $CuFe_2O_4$ photocatalyst degrades Rhodamine B at a rate of 94 percent. Consequently, the copper ferrite nanoparticles created by the combustion process using egg white as fuel serve as an excellent photocatalyst for Rhodamine B degradation.

The $OH^{\bullet}$ radical is the primary oxidant for Rhodamine B solution because it has a higher oxidation potential than hydrogen peroxide and ozone. The linked actions of electrons and holes cause decolourization and de-ethylation, resulting in degraded products such as N-de-ethylated intermediates, followed by hydroxylation, ring structure breaking, and further oxidation of these intermediates into acids, alcohols, and other low intermediates [30,31]. Finally, the acids, alcohols, and low intermediates mineralize entirely, releasing carbon dioxide, water, and inorganic nitrogen in the form of ammonium and nitrate ions. One of the initial phases in degrading Rhodamine B dyes is de-ethylation, followed by chromophore cleavage and the disintegration of the conjugated ring structure. Spinels are important in photocatalysis because they are typically produced as $A^{2+}B_23^{+}O_4$. In the spinel structure, the divalent Cu^{2+} ion occupies the A site position, while the trivalent iron ($Fe^{3+)}$ occupies the B site position. In addition to the methods described above, the Fe^{3+} cation on the surface of cobalt ferrite may react with hydrogen peroxide, generating a Fenton-like system that generates peroxide, •OOH, and OH• radials [32]. In this case, the number of hydroxyl radicals generated may be lowered because various reactions compete on the catalyst's surface. Furthermore, Fe^{3+} and H_2O_2 on the catalyst's surface may capture electrons generated in the copper ferrite system, resulting in OH• radicals. This method lowers electron-hole pair recombination, increasing photocatalytic degradation efficiency [33].

4. Conclusion

The present work focuses on the environmentally friendly manufacturing of copper ferrite nanoparticles utilising egg white as a precursor. Albumen from egg whites is used as fuel in the vehicle combustion process. According to the XRD results, the $CuFe_2O_4$ nanoparticles have a cubic spinel structure with a particle size of 37.3 nm. The existence of metal-oxygen vibration absorption peaks in the FTIR spectra at 477 and 566 cm^{-1} validates the spinel structure of copper ferrite. HRSEM and TEM micrographs highly indicated homogenous sphere aggregation with particle sizes ranging from 15 to 45 nm, corresponding to XRD results. In addition, Cu, Fe, and O were detected in the EDAX spectra of $CuFe_2O_4$ nanoparticles. UV DRS research reveals that the band gap of $CuFe_2O_4$ nanoparticles is 1.83 eV. The energy band diagram clearly shows that the produced $CuFe_2O_4$ nanoparticles may be employed for photocatalysis. Copper ferrite nanoparticles were discovered to be an excellent photocatalyst for Rhodamine B dye in visible light, with an efficacy of 94 percent, much more significant than copper ferrite nanoparticles made by chemical techniques.

Declaration of Competing Interest

The authors declared no conflict of interest

Acknowledgment: This work was funded by the Researchers Supporting Project Number (RSP2023R273) King Saud University, Riyadh, Saudi Arabia.

CRediT authorship contribution statement

P. Aji Udhaya: Conceptualization, Writing – original draft. **Awais Ahmad:** Writing – original draft, Writing – review & editing. **M. Meena:** Investigation, Project administration. **M. Abila Jeba Queen:** Data curation, Methodology. **M. Aravind:** Data curation, Resources. **P. Velusamy:** Data curation, Validation, Visualization. **Tahani Mazyad Almutairi:** Visualization, Conceptualization, Project administration. **Abdallah.A.A. Mohammed:** Visualization. **Shafaqat Ali:** Supervision, Conceptualization, Methodology, Project administration.

Data availability

No data was used for the research described in the article.

References

[1] E. Baldev, D. MubarakAli, A. Ilavarasi, D. Pandiaraj, K.S.S. Ishack, N &Thajuddin, Degradation of synthetic dye, Rhodamine B to environmentally non-toxic products using microalgae, Colloids Surf. B 105 (2013) 207–214.

[2] A.K. Moorthy, B.G. Rathi, S.P. Shukla, K. Kumar, V.S. Bharti, Acute toxicity of textile dye Methylene blue on growth and metabolism of selected freshwater microalgae, Environ. Toxicol. Pharmacol. 82 (2021) 103552.

[3] M.M. El-Sheekh, A.R. El-Shanshoury, G.W. Abou-El-Souod, D.Y. Gharieb, El Shafay, M S, Decolorization of dyestuffs by some species of green algae and cyanobacteria and its consortium, Int. J. Environ. Sci. Technol. 18 (12) (2021) 3895–3906.

[4] J.L. Snoek, Dispersion and absorption in magnetic ferrites at frequencies above one Mc/s, Physica 14 (4) (1948) 207–217.

[5] N. Kumari, S. Kour, G. Singh, R.K. Sharma, A brief review on synthesis, properties and applications of ferrites, AIP Conf. Proc. 2220 (1) (2020) 020164 AIP Publishing LLC.

[6] A. Vedrtnam, K. Kalauni, S. Dubey, A. Kumar, A comprehensive study on structure, properties, synthesis and characterization of ferrites, AIMS Mater. Sci. 7 (6) (2020) 800–835.

[7] Z. Sun, L. Liu, D. zeng Jia, W. Pan, Simple synthesis of $CuFe_2O_4$ nanoparticles as gas-sensing materials, Sens. Actuators B 125 (1) (2007) 144–148.

[8] L. Wang, D.C. Bock, J. Li, E.A. Stach, A.C. Marschilok, K.J. Takeuchi, E.S. Takeuchi, Synthesis and characterization of $CuFe_2O_4$ nano/submicron wire–carbon nanotube composites as binder-free anodes for Li-Ion batteries, ACS Appl. Mater. Interfaces 10 (10) (2018) 8770–8785.

[9] T. Dippong, E.A. Levei, O. Cadar, Recent advances in synthesis and applications of MFe_2O_4 (M= Co, Cu, Mn, Ni, Zn) nanoparticles, Nanomaterials 11 (6) (2021) 1560.

[10] S. Maensiri, C. Masingboon, B. Boonchom, S. Seraphin, A simple route to synthesize nickel ferrite ($NiFe_2O_4$) nanoparticles using egg white, Scr. Mater. 56 (9) (2007) 797–800.

[11] A.T. Dhiwahar, S. Maruthamuthu, R. Marnadu, M. Sundararajan, M.A. Manthrammel, M. Shkir, V.R.M. Reddy, Improved photocatalytic degradation of rhodamine B under visible light and magnetic properties using microwave combustion grown Ni doped copper ferrite spinel nanoparticles, Solid State Sci. 113 (2021) 106542.

[12] S.U. Bhasker, Y. Veeraswamy, N. Jayababu, M.V &Ramanareddy, Chromium substitution effect on the structural, optical, electrical and magnetic properties of Nickel ferrite nano particles; synthesized by an environmentally benign auto combustion method, Mater. Today Proc. 3 (10) (2016) 3666–3672.

[13] K. Shetty, L. Renuka, H.P. Nagaswarupa, H. Nagabhushana, K.S. Anantharaju, D. Rangappa, K. Ashwini, A comparative study on $CuFe_2O_4$, $ZnFe_2O_4$ and $NiFe_2O_4$: morphology, impedance and photocatalytic studies, Mater. Today: Proc. 4 (11) (2017) 11806–11815.

[14] L. Renuka, P. Mishra, Y.S. Vidya, G. Banuprakash, K.S. Anantharaju, K.N. Harish, Facile surface modification of Nickel ferrite nanomaterial by different routes: photoluminescence and photocatalytic activities, Mater. Today Proc. 46 (2021) 6022–6027.

[15] T. Ramaprasad, R.J. Kumar, U. Naresh, M. Prakash, D. Kothandan, K.C.B. Naidu, Effect of pH value on structural and magnetic properties of $CuFe_2O_4$ nanoparticles synthesized by low temperature hydrothermal technique, Mater. Res. Express 5 (9) (2018) 095025.

[16] J. Kurian, M.J. Mathew, A facile approach to the elucidation of magnetic parameters of $CuFe_2O_4$ nanoparticles synthesized by hydrothermal route, J. Magn. Magn. Mater. 428 (2017) 204–212.

[17] B.J. Rani, B. Saravanakumar, G. Ravi, V. Ganesh, S. Ravichandran, R &Yuvakkumar, Structural, optical and magnetic properties of $CuFe_2O_4$ nanoparticles, J. Mater. Sci. Mater. Electron. 29 (3) (2018) 1975–1984.

[18] Cullity, B.D. (1978). Diffraction under nonideal conditions. Elements of X-ray Diffraction, Addison-Wesley Publishing Company, 107–145.

[19] R. Lu, D. Yang, D. Cui, Z. Wang, L. Guo, Egg white-mediated green synthesis of silver nanoparticles with excellent biocompatibility and enhanced radiation effects on cancer cells, Int. J. Nanomed. 7 (2012) 2101.

[20] D.S. Nikam, S.V. Jadhav, V.M. Khot, R.A. Bohara, C.K. Hong, S.S. Mali, S.H. Pawar, Cation distribution, structural, morphological and magnetic properties of $Co_{1-x}Zn_xFe_2O_4$(x=0–1) nanoparticles, RSC Adv. 5 (3) (2015) 2338–2345.

[21] B. Issa, I.M. Obaidat, B.A. Albiss, Y. Haik, Magnetic nanoparticles: surface effects and properties related to biomedicine applications, Int. J. Mol. Sci. 14 (11) (2013) 21266–21305.

[22] A. Manikandan, J.J. Vijaya, L.J. Kennedy, M &Bououdina, Structural, optical and magnetic properties of $Zn_{1-x}CuxFe_2O_4$ nanoparticles prepared by microwave combustion method, J. Mol. Struct. 1035 (2013) 332–340.

[23] A. Manikandan, J.J. Vijaya, M. Sundararajan, C. Meganathan, L.J. Kennedy, M &Bououdina, Optical and magnetic properties of Mg-doped $ZnFe_2O_4$ nanoparticles prepared by rapid microwave combustion method, Superlattices Microstruct. 64 (2013) 118–131.

[24] M. Sundararajan, V. Sailaja, L.J. Kennedy, J.J. Vijaya, Photocatalytic degradation of rhodamine B under visible light using nanostructured zinc doped cobalt ferrite: kinetics and mechanism, Ceram. Int. 43 (1) (2017) 540–548.

[25] P. Nuengmatcha, S. Chanthai, R. Mahachai, W.C. Oh, Visible light-driven photocatalytic degradation of rhodamine B and industrial dyes (texbrite BAC-L and texbrite NFW-L) by ZnO-graphene-TiO_2 composite, J. Environ. Chem. Eng. 4 (2) (2016) 2170–2177.

[26] P. Zawadzki, M. Deska, Degradation efficiency and kinetics analysis of an advanced oxidation process utilizing ozone, hydrogen peroxide and persulfate to degrade the Dye Rhodamine B, Catalysts 11 (8) (2021) 974.

[27] S. Irfan, Z. Zhuanghao, F. Li, Y.X. Chen, G.X. Liang, J.T. Luo, F. Ping, Critical review: bismuth ferrite as an emerging visible light active nanostructured photocatalyst, J. Mater. Res. Technol. 8 (6) (2019) 6375–6389.

[28] M. Sundararajan, L.J. Kennedy, P. Nithya, J.J. Vijaya, M &Bououdina, Visible light driven photocatalytic degradation of rhodamine B using Mg doped cobalt ferrite spinel nanoparticles synthesized by microwave combustion method, J. Phys. Chem. Solids 108 (2017) 61–75.

[29] M. Pudukudy, Z. Yaakob, Facile synthesis of quasi spherical ZnO nanoparticles with excellent photocatalytic activity, J. Cluster Sci. 26 (4) (2015) 1187–1201.

[30] N. Nadeem, Q. Abbas, M. Yaseen, A. Jilani, M. Zahid, J. Iqbal, T. Jesionowski, Coal fly ash-based copper ferrite nanocomposites as potential heterogeneous photocatalysts for wastewater remediation, Appl. Surf. Sci. 565 (2021) 150542.

[31] P.N. Dayana, M.J. Abel, P. Inbaraj, S. Sivaranjani, R &Thiruneelakandan, Zirconium doped copper ferrite ($CuFe_2O_4$) nanoparticles for the enhancement of visible light-responsive photocatalytic degradation of rose Bengal and indigo carmine dyes, J. Cluster Sci. 33 (4) (2022) 1739–1749.

[32] N. Masunga, O.K. Mmelesi, K.K. Kefeni, B.B. Mamba, Recent advances in copper ferrite nanoparticles and nanocomposites synthesis, magnetic properties and application in water treatment, J. Environ. Chem. Eng. 7 (3) (2019) 103179.

[33] C. Singh, S. Bansal, V. Kumar, K.B. Tikoo, S. Singhal, Encrustation of cobalt doped copper ferrite nanoparticles on solid scaffold CNTs and their comparison with corresponding ferrite nanoparticles: a study of structural, optical, magnetic and photo catalytic properties, RSC Adv. 5 (49) (2015) 39052–39061.